The Ambient Seismic Field at Groningen Gas Field: An Overview from the Surface to Reservoir Depth

by Zack J. Spica, Nori Nakata, Xin Liu, Xander Campman, Zijian Tang, and Gregory C. Beroza

ABSTRACT

The long-term exploitation of the Groningen gas field led to compaction at reservoir depth, subsequent ground subsidence, and recently earthquakes. As part of an ongoing effort to quantify the hazard and risk in the region, several permanent and temporary seismic arrays have been deployed. As a result, the Groningen area is one of the seismologically best-instrumented areas worldwide. In this article, we describe several seismic experiments that were conducted in the region and take advantage of the numerous possibilities they offer to characterize the ambient seismic wavefield at the surface, in the shallow subsurface, and at reservoir depth. By means of beamforming, analysis of cross-correlation functions, surface-wave eigenfunction analysis, and correlations of neighboring frequencies, we are able to determine the main characteristics of the ambient seismic field (ASF), including the predominant propagation modes and phases. We retrieve clear multimode Rayleigh and Love waves, as well as and *P* waves, from cross correlations of the ASF. At reservoir depth, we show that the wavefield is largely trapped and reflected between geologic boundaries above and below the reservoir. This article reviews the characteristics of ASF observations with the goal of guiding future investigations of shallow structure of the Groningen area.

Electronic Supplement: Figure showing cross-correlation envelope functions between the two deep borehole arrays.

INTRODUCTION

The Groningen area in the northern Netherlands (Fig. 1) hosts one of the world's largest gas fields. Because of its long-term exploitation, the onshore gas field is subject to compaction at reservoir depth, and the resulting ground subsidence induces earthquakes (van Thienen-Visser and Breunese, 2015). To date, the largest earthquakes recorded in the region had local magnitude M_L 3.6 for the Huizinge earthquake of August 2012 and M_L 3.4 for the Zeerijp earthquake in January 2018, but larger magnitude earthquakes are possible (Zöller and Holschneider, 2016; Bommer *et al.*, 2017). In response to induced earthquakes, the Nederlandse Aardolie Maatschappij (NAM) and the Royal Netherlands Meteorological Institute (KNMI) are leading an extensive data acquisition and modeling program to quantify the seismic hazard and risk in the region (e.g., van Elk *et al.*, 2017). Part of this response includes the deployment and operation of a dense permanent borehole microseismic network covering an area of about 35 × 45 km (Fig. 1). This network is composed of ~70 accelerographs at the surface that are collocated with a borehole in which three to four geophones are installed at depth intervals of 30, 50, or 75 m. In addition, two deep borehole arrays with geophones at reservoir depth (i.e., ~3000 m) and several temporary nodal seismic experiments involving up to 415 three-component sensors were conducted by NAM. With such seismic networks covering an area of ~1600 km^2, the Groningen gas field is one of the seismologically best-instrumented areas on the Earth. In this study, we take advantage of the numerous possibilities offered by these different seismic networks to study the ambient seismic field (ASF) and to characterize the wavefield properties at the surface, in the shallow subsurface, and at reservoir depth. We cross-correlate the background ASF (sometimes called ambient noise) to obtain correlation functions that approximate the Green's functions of the medium between receivers (Shapiro and Campillo, 2004). By describing their different phases and the characteristics for the Groningen gas field, we intend this study to serve as the basis for future studies.

Over the last few decades, ASF interferometry has emerged as a powerful tool to image and monitor the Earth's interior. Fundamental-mode surface waves (Rayleigh and Love waves) are now routinely extracted from ASF to image the crust, the lithosphere, and the upper mantle (e.g., Bensen *et al.*, 2008) at global (Nishida *et al.*, 2009), regional (Shapiro *et al.*, 2005), and local scales (e.g., Spica, Perton, and Legrand, 2017). Body-wave retrieval is more challenging; however, recent exam-

doi: 10.1785/0220170256

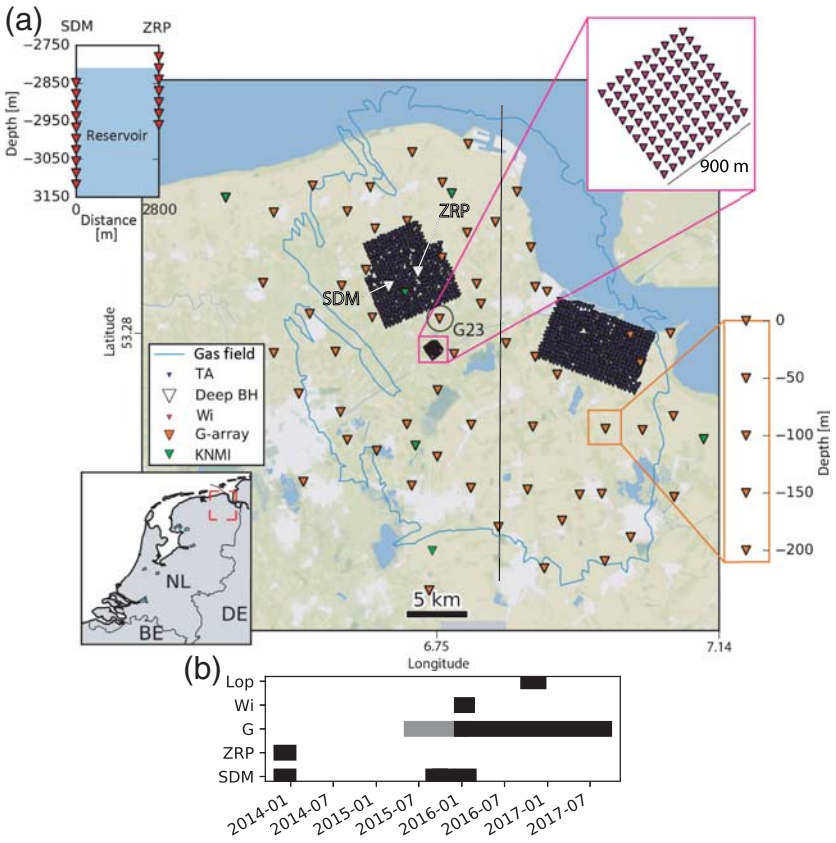

▲ **Figure 1.** (a) Map view of the Groningen gas field area. White areas depict urban centers. The location of the Groningen gas field in the northern part of the Netherlands is shown in the map in the lower left corner of the figure (red contour). The blue contour depicts the outline of the gas field. The vertical gray dashed line depicts the location where the section of the velocity model shown in Figure 2a has been taken. Orange triangles depict the G-array. The 1D velocity model at station G23 (encircle) is shown in Figure 2b. Vertical view of one shallow borehole of this array is shown in the orange box on the right side. Green triangles depict the borehole array operated by the Royal Netherlands Meteorological Institute (KNMI) since 1991. The pink box on the map is zoomed in the upper right corner of the figure. It depicts the Wittewierum array and its 100 vertical-component geophones. It is reported as "Wi" in the legend of the figure. Small blue triangles depict the Loppersum (northern) and Borgsweer (eastern) arrays. They are reported as "TA" (standing for Transportable Array) in the legend of the figure. Two white triangles in the middle of the Loppersum array depict the deep borehole arrays, namely SDM (western) and ZRP (eastern). A vertical view of these arrays at reservoir depth is shown in the upper left corner of the figure. (b) Summary of the start and end times of the different arrays used in this study. G, G-array; Wi, Wittewierum; Lop, Loppersum. SDM and ZRP are the two deep borehole arrays. The gray rectangle corresponds to a period when the G-array was under construction.

ples attest to that possibility (e.g., Roux *et al.*, 2005; Ruigrok *et al.*, 2011; Poli *et al.*, 2012; Nakata *et al.*, 2015; Spica, Perton, Nakata, *et al.*, 2017). In active producing fields (oil, gas, or geothermal), ASF interferometry of geophones in boreholes is emerging as a method well suited for permanent reservoir monitoring (e.g., Hillers *et al.*, 2015; Behm, 2017) or to assess the *P*- and *S*-velocity structure of such reservoirs (e.g., Miyazawa *et al.*, 2008; Zhou and Paulssen, 2017). Trapped waves in the ASF between geological boundaries can also be used to quantify certain of the reservoir characteristics. Previous studies have shown fault-zone-trapped modes (Hillers *et al.*, 2014; Hillers and Campillo, 2016), but in this study, we show for the first time an example of such a trapped ASF wavefield inside a gas reservoir.

An important requirement for successful ASF interferometry is that the ASF sources are of equal strength and homogeneously distributed around the seismic network (Wapenaar and Fokkema, 2006). Although it is well known that the distribution of sources of ASF is inhomogeneous (Stehly *et al.*, 2006), the situation can be improved by correlating ASF over long time periods (Sánchez-Sesma and Campillo, 2006). The frequency bandwidth and the modal structure of the cross-correlation functions are highly dependent not only on the sources and the medium but also on the properties of the seismic network. Receiver spacing is a consideration because the coherent propagating ASF must have sufficient energy to be recorded on both receivers despite geometrical spreading and attenuation. Because most ASF energy propagates as surface waves (Aki and Richards, 2002; Bonnefoy-Claudet *et al.*, 2006) and because surface waves are slowly attenuated, they dominate the signal in the estimated Green's functions. Because the Earth's upper crust is highly heterogeneous, a fraction of this energy is locally converted into body waves (Roux *et al.*, 2005); however, body waves lose amplitude more quickly due to faster geometrical spreading. Therefore, dense nodal arrays are potentially better suited to retrieve direct body waves because the coherency of ASF between stations is higher and extends to higher frequency. Having sensors at depth is an alternative for better retrieval of body waves because deeper sensors will reduce the dominance of surface-wave modes with large amplitudes.

The seismic arrays at Groningen offer a unique opportunity to study the ASF with a variety of configurations in a single geological setting. This study aims to provide an outline of the different seismic waves that can be retrieved using the various array combinations in the Groningen gas field. It also provides some information about the possible direction of sources of the ASF in the region. As an overview useful for future ASF-based studies, we provide geological information about the region, followed by some technical information about various seismic experiments (permanent and temporary) conducted in the Groningen area. We then show

beamforming results over different surface arrays to study the incidence of the incoming ASF over a broad range of frequencies. We also present correlation functions at shallow depths and show that Rayleigh, Love, and P waves can be retrieved with the permanent seismic network. We finish by showing and discussing atypical ASF correlation results obtained between the shallow surface and the reservoir and also directly at reservoir depth using two deep borehole arrays.

GEOLOGICAL SUMMARY AND VELOCITY MODEL MAIN CHARACTERISTICS

We provide here some basic elements of the geology of the Groningen area to interpret the velocity model shown in Figure 2. For a complete description of the different formations and their history, we invite the reader to consult the following references: De Mulder *et al.* (2003) and Vos (2015); or the Dinoloket website (see Data and Resources).

The Groningen area is characterized by flat topography with altitude close to mean sea level. The shallowest horizons are included in the North Sea Supergroup, itself including the Upper, Middle, and Lower North Sea Groups. It consists of an ~800−m−thick layer that includes Paleogene, Neogene, and Quaternary deposits (De Mulder *et al.*, 2003; Vos, 2015). It comprises unconsolidated sediments ranging from fluvial braids, plain sands to shallow marine (intertidal), and terrestrial deposits of soft clays to distinct organic-rich peat formations. Recent studies highlighted the large degree of vertical and lateral heterogeneity in this shallow part of the area (i.e., first hundreds of meters; Hofman *et al.*, 2017; Kruiver *et al.*, 2017; Spica, Perton, and Beroza, 2017; Noorlandt *et al.*, 2018; Spica *et al.*, 2018). The Lower North Sea Group overlays the Chalk Group, composed of bioclastic limestones and marly limestones from the Upper Cretaceous. The base of this group lies atop the Rijnland Group that is mainly composed of argillaceous formations of Late Ryazanian to Albian. It overlays the Jurassic deposits composed of a succession of marine claystones, siltstones, marls, and some sandstones that have been placed in the Altena Group. Then, the Triassic deposits are part of the Upper Germanic Trias Group and composed of alternating clastics, carbonates, and evaporites. The gas reservoir is located inside the Upper Permian deposits at an average depth of ~3000 m. It belongs to the Upper Rotliegend Group and is located just under a salt and anhydrite layer.

All these geological units are highlighted in Figure 2a, which is a vertical slice over the 3D V_P velocity model provided by the NAM. This velocity model was first obtained from active 3D seismic data conducted in the 1990s during the development of the gas field and then constantly updated by NAM. Figure 2b depicts a 1D velocity (V_P and V_S) and density model extracted from the 3D model at the shallow borehole site G23. An important feature of the velocity model is that the seismic velocities at reservoir depth sharply drop to much lower values. This makes the precise location of earthquakes recorded at reservoir depth difficult (e.g., Ruigrok *et al.*, 2015) due to the strong reverberation of the waves against the walls of the reservoir. As described in this study, the sharp velocity contrasts in this model appear to have a strong influence on the ASF as well.

SEISMIC ARRAYS OVERVIEW

The G-Array

Since 1991, the Groningen area has been seismically monitored by a borehole seismometer network under the maintenance of the KNMI (green triangles in Fig. 1). In 2015, this array was complemented by the G-array, which is the backbone borehole array that continuously monitors the Groningen gas field (orange triangles in Fig. 1). It consists of a network of ~70 accelerometers at the surface that are paired with ~200 m boreholes in which four short-period stations (4.5 Hz natural frequency) are located at depth intervals of 30, 50, or 75 m. The installation of the network started in 2015 and it was fully operational in January 2016. Recordings of continuous waveforms are freely available on the KNMI website. The network was operational during all the temporary experiments described below (KNMI, 1993).

The Deep Borehole Arrays

Two deep boreholes arrays (white triangles in Fig. 1) are located 2800 m apart. SDM, the western deep borehole array, is composed of 10 three-component 15 Hz geophones, all located inside the gas reservoir evenly spaced from 2850 to 3100 m depth. ZRP, the eastern deep borehole array, is composed of 7 three-component 15 Hz geophones for which two stations are located above the reservoir and all the others are inside the reservoir, from 2800 to 2950 m depth. Because of their depth and the physical conditions at depth (i.e., pressure and temperature), the maintenance of these arrays is challenging and recording is not continuous. In this study, we take advantage of one time period when both arrays were operational to compute cross correlations between these two arrays (Julian days 326–357 of the year 2013) and another period when SDM and the G-array were both operational to compute cross correlations between reservoir and the shallow surface (September, October 2015, and January 2016).

The Wittewierum Array

This array consists of 100 vertical-component 5 Hz geophones evenly spaced at 100 m on a square grid (pink triangles in Fig. 1). It was temporarily installed in the central region of the Groningen gas field for ~22 days in January 2016.

The Loppersum and Borgsweer Arrays

The Loppsersum and Borgsweer arrays are the first and second phases, respectively, of the Groningen transportable three-component nodal array experiment (blue triangles in Fig. 1). The transportable array features 415 stations with 5 Hz natural frequency almost evenly spaced at ~350 m in these first two deployments. During the first phase of the experiment, stations were deployed for 45 days (Julian days 284–329 of the year 2016) in the Loppersum region, which is north of the Wittewierum array. In this study, we only use data from the

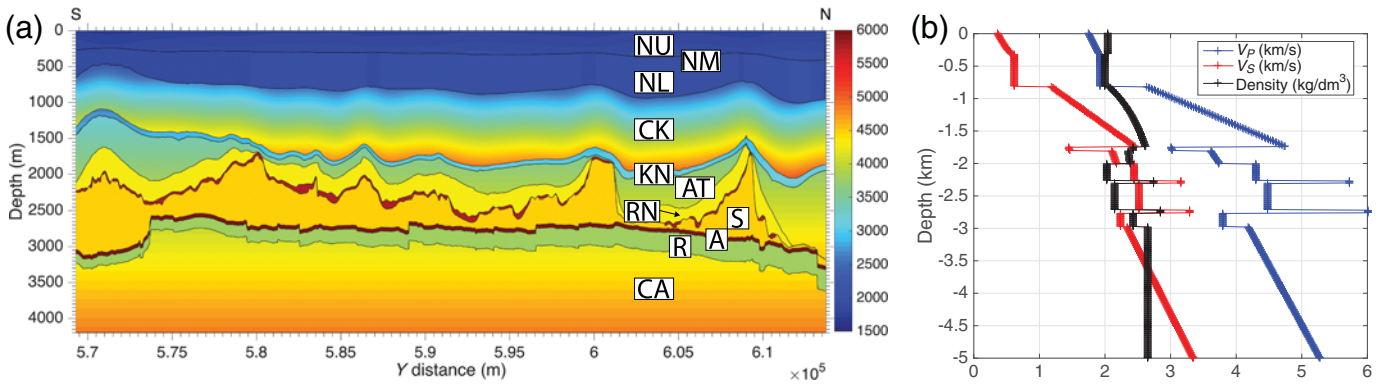

▲ **Figure 2.** (a) 2D slice inside the V_P velocity model (May 2015) provided by Nederlandse Aardolie Maatschappij (NAM). NU, Upper North Sea Group; NM, Middle North Sea Group; NL, Lower North Sea Group; CK, Chalk Group; KN, Rijnland Group; AT, Altea Group; RN, Upper Germanic Trias Group; S, salt layer; A, basal anhydrite; R, reservoir; CA, Carboniferous. (b) 1D V_P, V_S, and ρ model extracted at borehole site G23. ρ is derived from *P*-wave velocity using the empirical relationships provided by NAM.

Loppersum array but all the results shown for the Loppersum array have been confirmed by the analysis of the Borgsweer array. The Borgsweer array was deployed over the eastern part of the gas field. Since Borgsweer, this array has been moved several times over the entire field and up to 11 phases are expected to be conducted, with different configurations.

Data Availability and Noise-Level Analysis

An overview of the data available and used in this study is shown in Figure 1b. For an overview of the noise level at different arrays, we computed the power spectral density (PSD) functions (Kay, 1988). We conducted this analysis for all the stations at different depth levels for site G23 (see Fig. 1), for one station inside the deep borehole SDM (inside the reservoir), for several stations of the Loppersum array, and for several stations of the Wittewierum array. The results are shown in Figure A1 and discussed in Appendix A. One notable finding of this analysis is that the level of noise is high at almost all stations and frequencies, likely because of the vicinity of the Groningen area with the North Sea. Also, although the natural frequencies of the shallow borehole and surface geophones are 4.5 and 5 Hz, we are able to retrieve ground movements down to much lower frequencies (at least 0.1 Hz). This is not the case for the deep borehole arrays where strong instrumental noise seems to dominate the records down to 10 Hz; however, in our analysis (see the Retrieved Wavefield at Reservoir Depth section) we show that actual ground movement is still extractable from correlations at much lower frequencies for these arrays. This is possible as long as the noise level occasionally reaches above the least-significant bit of the recorder, with sufficiently long averaging times.

PROPERTIES OF THE AMBIENT SEISMIC FIELD AT THE NEAR SURFACE

Beamforming

Because our goal is to determine what wave types can be retrieved from ASF in Groningen, we first study the directionality of the ASF energy through a beamforming analysis. To gain in resolution over a broad range of frequencies, we take advantage of the G-array (at 50 m depth level), the Loppersum array, and the Wittewierum array, all of which have different size and geometry and sample accurately different frequency ranges (see Appendix B). Array responses for each of these arrays are shown in Figure B1. As expected, synthetic tests show that lower frequencies are better sampled using the G-array (0.125, 0.2 Hz), whereas intermediate (0.5, 1.0 Hz) and higher frequencies (1.5, 2.0 Hz) are better retrieved with the Loppersum and Wittewierum arrays, respectively (see Appendix B for a complete description).

We apply plane-wave beamforming in the frequency domain following Lacoss *et al.* (1969). To reduce the effect of strong incoming waves (e.g., earthquakes) and site amplification, we normalize the signal in each window of 1 hr and in each frequency band by its maximum amplitude before stacking. Beamforming computed in distinct frequency bands for the vertical component are shown in Figure 3.

At the primary and secondary microseism frequencies (i.e., 0.08 and 0.125 Hz), strong surface-wave energy comes mainly from the west with a velocity of about 2–5 km/s. Most of the energy spreads over a large back-azimuth range. At 0.2 Hz, we observe a southwest directionality of the energy traveling through the G-array. Because the beamforming was computed with 30 days of ASF recorded in January 2016, storms near the British coast (e.g., Kimman *et al.*, 2012) or in the Atlantic might be the sources of energy at that frequency and explain the large back-azimuth range. At intermediate frequencies (i.e., 0.5 and 1 Hz) surface-wave (fundamental and higher modes of the Rayleigh wave) energy likely comes from the North Sea with a velocity of about 0.5–1 km/s. This interpretation is supported by the results of Kimman *et al.* (2012) who observed a similar feature at 0.4 Hz. At higher frequencies (1.5 and 2.0 Hz), surface waves sample the shallowest part of the subsoil, and their velocity is as low as 0.4 km/s. Even though the strongest energy still comes from the direction of the North Sea, wave arrivals are observed over almost all azimuths,

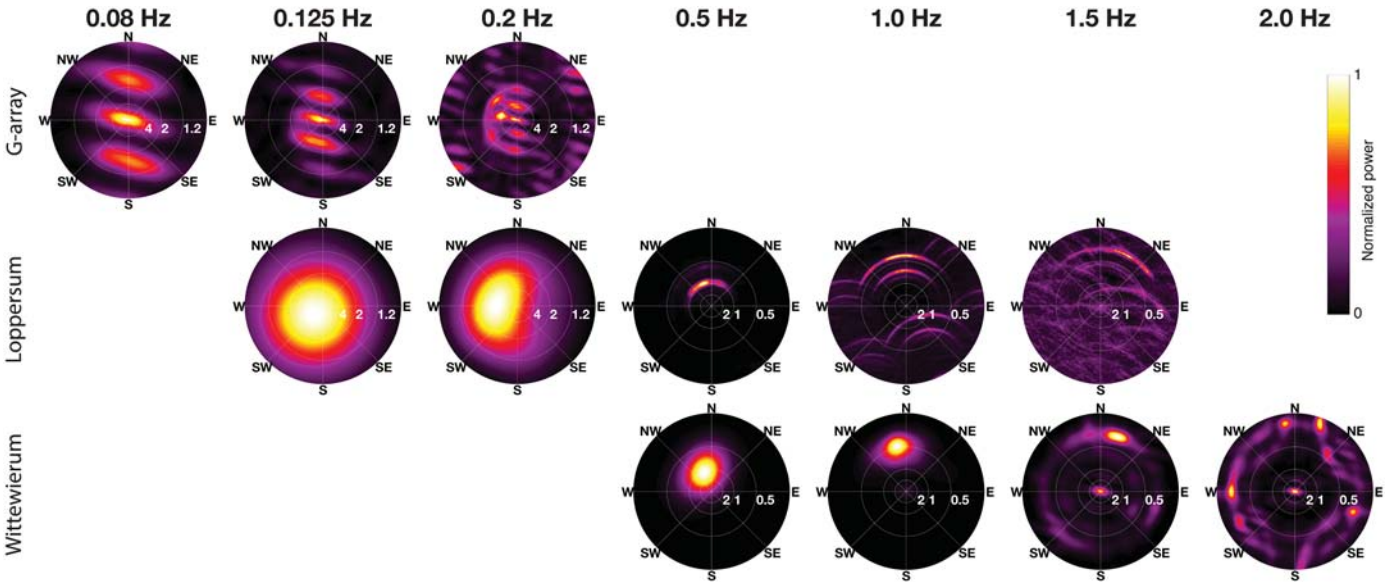

▲ **Figure 3.** Beamforming results using ambient seismic field (ASF) recordings from the G-array, Loppersum array, and Wittewierum array in different frequency bands. The power of observed ASF at each array in the horizontal slowness domain is averaged over 30, 42, and 19 days for the G-, Loppersum, and Wittewierum arrays, respectively. For both the Loppersum and Wittewierum arrays, the entire data set was used. For the G-array, we used data overlapping in time with the Loppersum array. Bright colors indicate a direction of strong incoming energy. Amplitudes are normalized to their maximum in each panel. The numbers at each white circle indicate the corresponding velocity in km/s. Note that the slowness axes are smaller for frequencies under 0.5 Hz. Spaces are left blank when beamforming results are uninformative due to array limitations, as described in Appendix B.

suggesting a strong anthropogenic contribution, strong scattering, or both.

Ambient Seismic Field Correlation Functions

For the following analysis, we obtained cross-correlation functions by computing power-normalized cross correlations (cross coherence) between all receiver pairs in the frequency domain (e.g., Nakata *et al.*, 2013). We removed instrumental response prior to correlation. In addition to vertical–vertical (ZZ) component, we compute also the north–north (NN), north–east (NE), east–east (EE), and east–north (EN) as well as the transverse–transverse (TT), transverse–radial (TR), radial–radial (RR), and radial–transverse (RT) cross correlations, for which we applied a tensor rotation, prior to correlation. We then used a linearly interpolated stack to create binned stack gathers (superstack gathers; Claerbout, 2014). In this processing, we implicitly assume a 1D layered medium.

Using the G-Array

We cross-correlated the ASF for all combinations of receiver pairs of the G-array between 19 August 2015 and 10 May 2016. In Figure 4, we show the bin-stacked correlation functions of the nine components for only the surface stations of the G-array and for reference station G410, band-pass filtered between 0.25 and 0.5 Hz. In Figure 5, we show binned stack gathers for all correlation functions obtained at different borehole levels for ZZ and TT components.

As expected, the ZZ, ZR, RZ, RR, and TT components in Figure 4 show much more coherent wave energy than other components. This is attributable to the fact that the ZT, TR, RT, and TZ components will all reflect *P–SV* to *SH* coupling due to laterally varying structure and/or anisotropy. Because the predominant structure is horizontal layering, such arrivals are naturally suppressed.

In the ZZ component of Figure 4, we observe a Rayleigh wave with a velocity of ~1.6 km/s and another Rayleigh wave with a much lower velocity of ~0.8 km/s. In the RR component, the Rayleigh wave has stronger amplitude. In Figure 5a in the ZZ component at 0.125–0.25 Hz, we observe that the ~1.6 km/s Rayleigh wave has an amplitude that stays fairly constant with depth. On the other hand, the ~0.8 km/s surface wave in the higher frequency band (0.5–1.0 Hz; in Fig. 5b) is stronger at the surface, and its amplitude decays with depth. Surface-wave eigenfunction analysis (see the Surface-Wave Eigenfunction Analysis section) suggests that this wave is the fundamental-mode Rayleigh wave. At a short period, this wave is likely trapped in the near surface, which explains the amplitude observations.

On the TT component (0.25–0.5 Hz in both Figs. 4 and 5c), we observe a clear wave packet with a velocity of about 1.8 km/s. The apparent dispersion suggests that it corresponds to Love waves. The amplitudes of these waves do not vary much with depth, which is consistent with the Love wave eigenfunction analysis in the Surface-Wave Eigenfunction Analysis section.

We observe a wave traveling at ~300 m/s in Figure 5b,c. This wave, which might be an air wave or tube wave, is amplified with depth for the ZZ component, whereas its amplitude remains constant with depth for the TT component. Interestingly, Figure 5a,b shows a clear *P* wave, traveling at

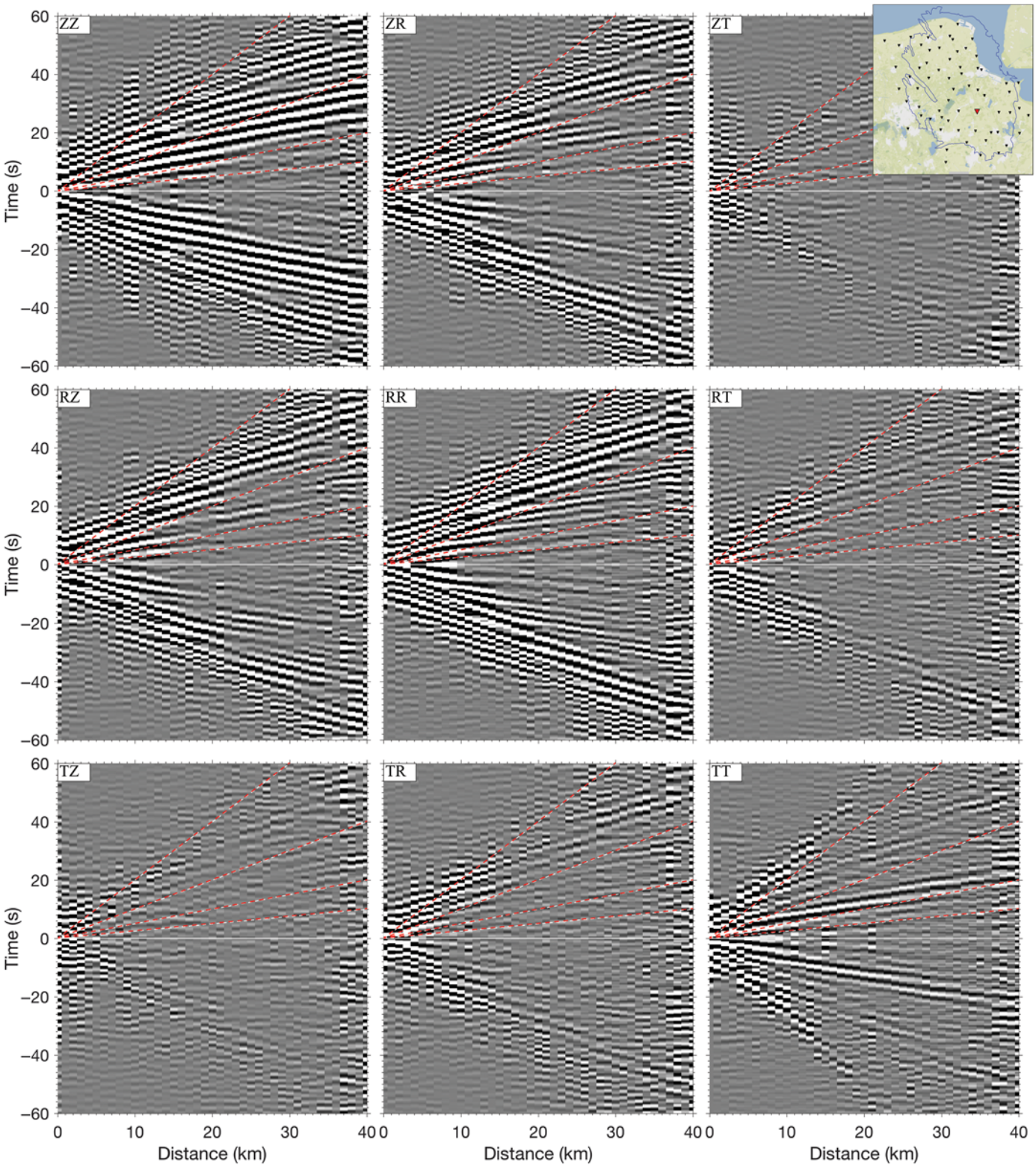

▲ **Figure 4.** Bin-stacked correlation functions for the nine components, with reference station G410 highlighted by the red inverted triangle in the map in the upper right corner. In the component of each subplot, the first letter refers to the receiver component and the latter to the virtual source component. Red dashed lines are the travel times of waves with velocities of 0.5, 1, 2, and 4 km/s. The frequency range is 0.25–0.5 Hz. The amplitude balance is preserved among all panels, and the bin size in 1000 m.

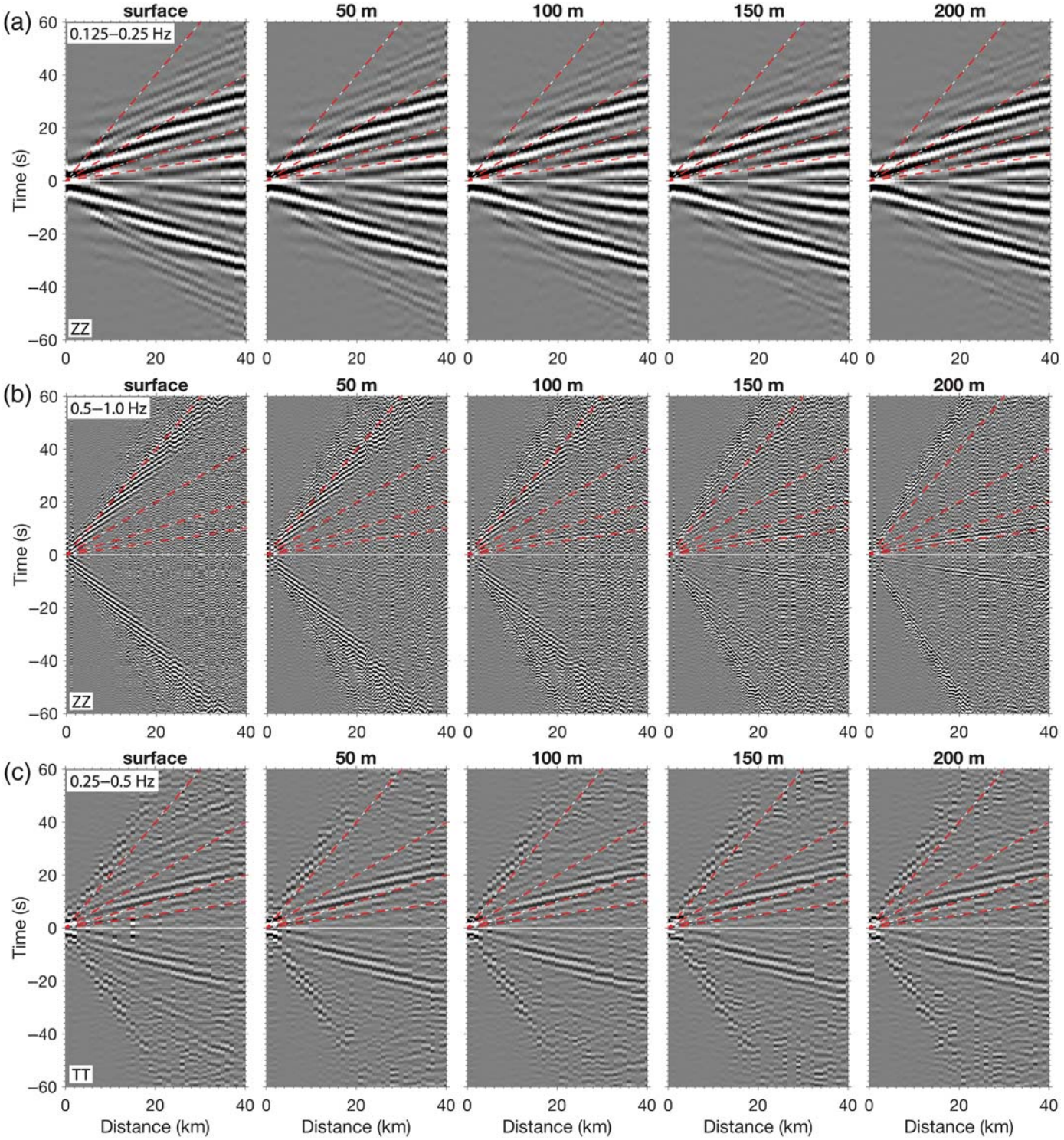

▲ **Figure 5.** Bin-stacked correlation functions for (a,b) ZZ and (c) TT components at different depths and different frequency ranges. Red dashed lines are the travel times of waves with velocities of 0.5, 1, 2, and 4 km/s. The bin size is 1000, 250, and 1000 m for (a–c), respectively.

3.5–4.0 km/s. Although its amplitude is fairly constant with depth in the 0.125–0.25 Hz frequency band, its signal-to-noise ratio (SNR) appears to be higher with increasing depth in the 0.5–1.0 Hz frequency band.

Using the Loppersum Array

In Figure 6, we show bin-stacked correlation functions in the time–space domain and in the frequency–phase velocity domain for the nine components and computed using the Loppersum

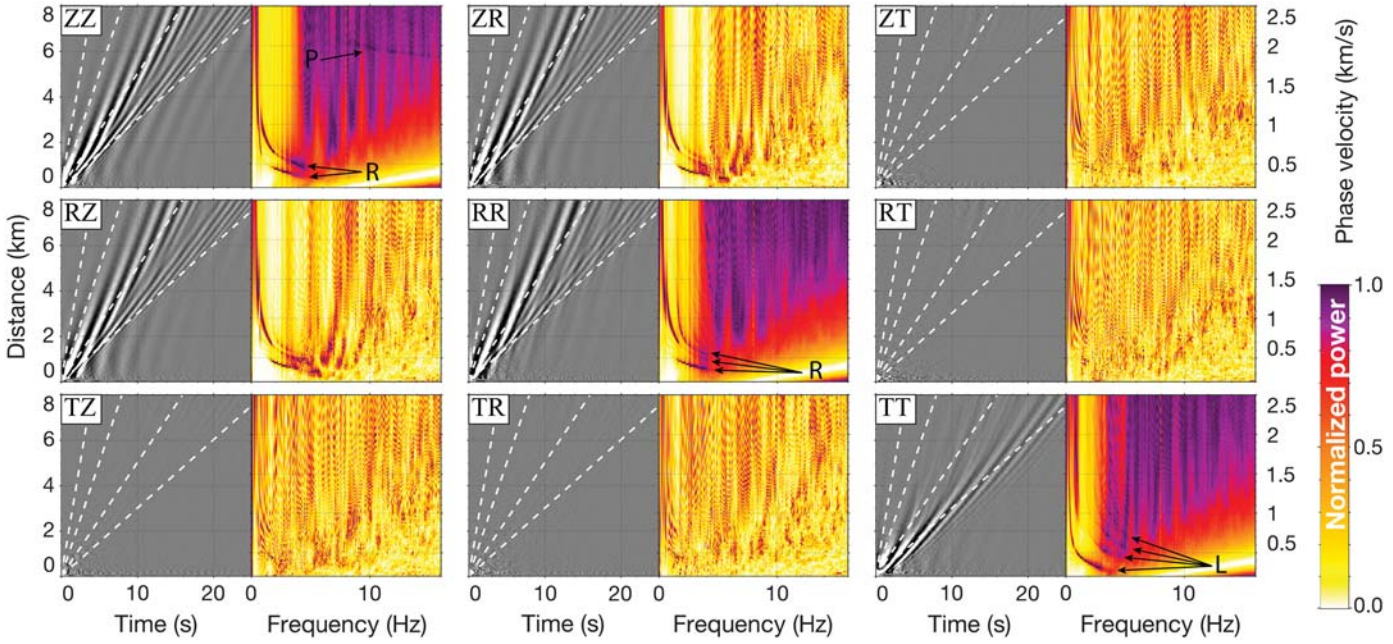

▲ **Figure 6.** Bin-stacked raw correlation functions in the (left) time–space domain and (right) frequency–phase velocity domain at each component. The first and second letters of the component notation indicates the components on the receiver and source sides, respectively. Red dashed lines show the travel time of the waves with velocities of 2, 1, 0.5, and 0.3 km/s with straight path. In the time-domain panels, amplitudes of each panel are normalized by the same factor; the relative amplitudes between panels are preserved. In the frequency-domain panels, each panel is individually normalized. In panels ZZ, RR, and TT, the letters P, R, and L stand for *P*, Rayleigh, and Love waves, respectively.

array. In the time domain, the basic features in the correlation functions are similar to what we found within the G-array (Figs. 4 and 5) or in the slowness plots from beamforming (Fig. 3); however, the high number of stations, the shorter interstation distances and the frequency–phase velocity analysis allow us to gain a more detailed understanding of wave phenomena.

On the ZZ component, we observe Rayleigh waves with two strong wave modes propagating with group velocities of 0.3 and 0.5 km/s. Both waves propagate through the entire array through the largest offset of 8 km. As observed in the beamforming results (Fig. 3) and frequency–phase velocity maps (Fig. 6), the phase velocities are much larger than group velocities. These modes are observed from 0.2 to 4.5 Hz. Therefore, we observe coherent waves with much wider frequency range than using beamforming because cross correlation is not subject to cycle-skipping effects. On the RR component, we observe up to the second higher mode of Rayleigh over a limited frequency range.

P waves are observed on the ZZ component at 1.8–2.0 km/s. These waves have high SNR from 7 to 15 Hz. In Figure 6 (ZZ), it appears that the *P* waves present some frequency-dependent propagation, which is very peculiar. We hypothesize that this apparent frequency-dependent propagation is due to the fact that the high-frequency waves are extracted in only short interstation distance pairs; therefore, the *P* wave propagates at the shallower structure, which has slower velocities than deeper structure. Hence, the apparent frequency-dependent propagation in the frequency panel should be interpreted as the *P*-wavepath depth variation manifest in the stacking process rather than a true dispersion of seismic velocities.

The fundamental mode of the TT component is much stronger than the higher modes, although multiple higher modes are also extracted with up to the third higher mode in the power spectra. The frequency range of the fundamental mode is 0.3–4.0 Hz, and higher modes are about ~3–5 Hz; however, *S* waves are not clearly extracted. Because the reverberations of *SH* waves asymptotically merge with Love waves, and Love waves are clearly observed, *S* wave signals may be present at small offsets. The presence of multiple higher Love modes indicates that we should have substantial sensitivity to and the potential for resolution of vertical *SH* wavespeeds. To our knowledge, this is the first time for observation of so many higher modes in ambient field data. It illustrates both the high quality of the data and the richness of the ASF at Groningen.

As observed in Figure 4, the other components (RT, ZT, TZ, and TR) do not show strong coherent waves, and the amplitudes of these components are much smaller than the ZZ, ZR, RZ, RR, and TT components.

Using borehole interferometry, Hofman *et al.* (2017), Spica, Perton, Nakata, *et al.* (2017), and Noorlandt *et al.* (2018) retrieved *P* and *S* waves inside the G-array's boreholes and Zhou and Paulssen (2017) characterized *P*- and *S*-wave velocities of the reservoir using borehole interferometry using the SDM and ZRP arrays.

Table 1 presents a summary of our observations related to the retrieved wavefield based on ASF correlations in the near

Table 1
Summary of the Retrieved Wavefield from Ambient Seismic Field Correlations at Groningen in the Near Surface

	Frequency (Hz)	Distance (km)	Apparent Velocity (km/s)	Remark
Rayleigh	0.1–1.0	0.05–60	0.7–1.6	Primarily on ZZ and RR; up to second-higher mode
Love	0.1–1.0	0.5–60	1.8–3.0	Primarily on TT; up to third-higher mode
P wave	0.4–16.0	0.5–20	2.0–4.0	> SNR at depth with binning stack

Frequency content, interstation distance, and apparent velocity are average values that might change slightly for different station combinations. ZZ, vertical–vertical; RR, radial–radial; SNR, signal-to-noise ratio.

surface. In the Properties of Ambient Seismic Field at Reservoir Depth section, we show and discuss atypical correlation combinations that involve the deep borehole arrays inside the reservoir.

PROPERTIES OF AMBIENT SEISMIC FIELD AT RESERVOIR DEPTH

Retrieved Wavefield between the Reservoir and the Surface

We use three months of continuous data to compute cross-correlation functions (cross coherence, as in the Ambient Seismic Field Correlation Functions section) between ZZ, RR, and TT components. In Figure 7a,b, we show the results as single virtual-source correlation plots (i.e., one station vs. all others, sorted by interstation distance and with no spatial averaging) for the reference stations SDM–010 (the deepest of the SDM array) with all stations of the G-array at 200 m depth and for frequency bands of 0.125–0.5 and 0.5–1 Hz, respectively.

For the lower frequency band, we observe fairly clear arrivals on the ZZ component, which are Rayleigh waves with an apparent velocity of ~1–2 km/s. The correlation functions appear reasonably symmetric in the ZZ component but the symmetry is nearly absent in other components and/or at larger distances. Beyond the Rayleigh waves, we observe a weak arrival on the TT component with an apparent wavespeed of ~2 km/s, which is slightly lower than the *S*-wave velocity at reservoir depth (i.e., ~2.2 km/s). Although it likely depicts Love waves, the poor SNR of these waves makes confirmation difficult. Overall, the SNR of these correlation functions is much lower than for those observed for G-array correlations shown in Figure 5. Furthermore, we note that no coherent arrivals are observed in the 0.5–1.0 Hz frequency band (Fig. 7b), which also differs from previous analysis at shallower depth. This behavior is well illustrated in Figure 7c, which depicts the amplitude spectra of the same correlation functions, sorted by distance. It shows that no information is retrieved at periods below 2 s, regardless of the interstation distance or the components computed. This strong decay below 2 s is observable in all the amplitude spectra.

Surface-Wave Eigenfunction Analysis

To understand better why the ASF below 2 s is uncorrelated and why this contrast is so sharp, we examine in Figure 8 the expected surface-wave eigenfunction given a reference velocity model. We follow Denolle *et al.* (2012) to compute the surface-wave eigenfunctions (Appendix C), and we use the 1D depth-dependent *P*, *S* velocity, and density model extracted from a location near shallow borehole G23 as a reference (Fig. 2b). The top 5 km of the 1D depth model is divided into a stack of layers with a constant velocity of 10 m thickness. The velocity and density values below 5 km depth are assumed constant. Interfaces are defined to account for discontinuities in velocity and density. We compute both fundamental and first higher modes for each displacement eigenfunction component.

In agreement with the observations in Figure 7, the eigenfunction sensitivity explains why we cannot retrieve clear propagating surface waves from the ASF correlation using the deep borehole arrays at periods shorter than 2 s. The characteristics of the velocity structure at Groningen, which includes a salt layer and various strong velocity contrasts or wave guides (see the Geological Summary and Velocity Model Main Characteristics section) has a strong influence on the surface-wave energy with depth, leading to an absence of coherent surface-wave energy at high frequencies at reservoir depth. This means that the relatively small earthquake sources observed so far in the Groningen reservoir should not generate high-frequency fundamental-mode surface waves.

Coherency of the Ambient Seismic Field at Shallow and Reservoir Depths

Even if the surface-wave energy is weak, high-frequency ASF is present at reservoir depth (Zhou and Paulssen, 2017); however, it appears that these frequencies are poorly correlated with the ASF at the surface. We follow Liu and Ben-Zion (2016) to understand the correlation structure among neighboring frequencies in the ASF data. We estimate the correlation coefficient of power spectral values at neighboring frequencies for the deep borehole station ZRP–010 and shallow borehole G421 (see Appendix D). Each element in the matrix is computed using power spectral values at corresponding frequencies over numerous time windows. The correlation between different frequency components is an indicator of the diffusiveness of the wavefield and provides additional information on the noise sources and propagation regime at a given frequency range.

In Figure 9a,b, we show the correlation matrix obtained for ZRP–010 for different frequency ranges. We observe that the matrix is diagonally dominant for low frequencies below 1.5 Hz, meaning that these frequencies are not correlated, which suggests a diffuse wavefield at reservoir depth. We

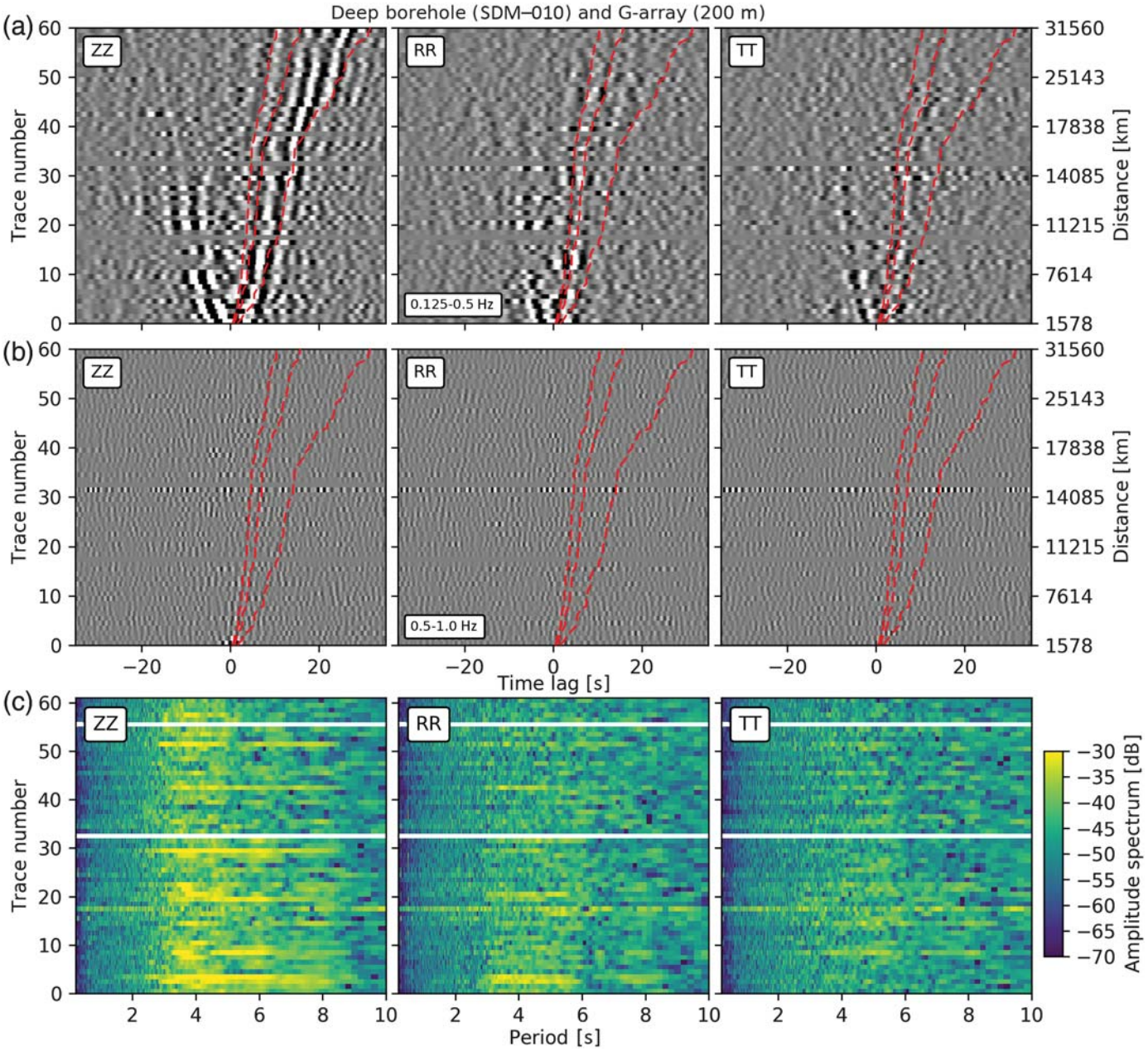

▲ **Figure 7.** (a,b) Correlation functions for the ZZ, RR, and TT components with reference station SDM–010 and all the stations of the G-array at 200 m depth, sorted by distance from the deep borehole. From inside to outside, red dashed lines are the travel times of waves with velocities of 1, 2, and 3 km/s. In (a), the frequency range is 0.125–0.5 Hz. In (b), the frequency range is 0.5–1.0 Hz. The amplitude balance is preserved among (a,b). Note that similar results are observed when correlating SDM–010 and all the stations of the G-array at the surface. (c) Amplitude spectra of the computed correlation functions for the ZZ, RR, and TT components as a function of interstation distance from the deep borehole (SDM–010) and all the stations of the G-array at 200 m depth.

observe weaker correlations (less than 0.2) at around 1.7 Hz and between 4 and 5 Hz. These weaker high frequencies recorded at reservoir depth are likely reflecting anthropogenic sources from the surface (Gupta, 1965; Douze, 1967; Zhou and Paulssen, 2017).

In Figure 9c, we show the correlation matrix obtained for station G421 at 50 m depth. The matrix shows significant correlations between neighboring frequencies near 0.25 Hz (Fig. 9c). This indicates a strong nondiffuse ASF component from the ocean (Liu and Ben-Zion, 2016), which provides further support for a different behavior of the ASF between the surface and the reservoir.

Because the long-period (> 5 s) ASF still has energy at reservoir depth (Fig. 8a), the observed more-diffuse ASF at depth could be related to complex geological structure that might induce stronger scattering at depth than the materials

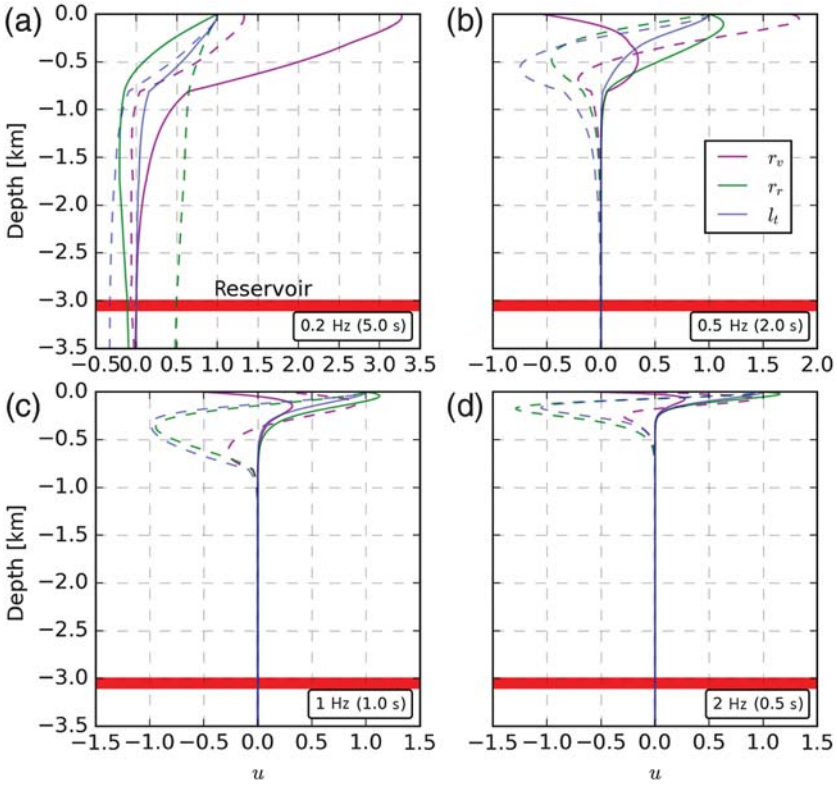

▲ **Figure 8.** Panels (a–d) correspond to surface-wave eigenfunctions at periods 5, 2, 1, and 0.5 s, respectively. Both fundamental (solid lines) and first higher mode (dashed lines) for Rayleigh (r_v and r_r—vertical and radial, respectively) and Love (l_t—transverse) waves are shown. The red horizontal line depicts the approximate depth of the gas reservoir. As expected, short-period eigenfunctions (i.e., 0.5, 1 s; panels c and d) sample shallower depth (< 1 km depth) than at longer period (i.e., 5 s; panel a). At 2 s, surface waves do not sample depths greater than ~1.5 km (panel b). At 5 s, surface-wave energy is extremely weak for depths greater than ~1.5 km.

in the near-surface. Another possibility could be that the deep geophones with a resonant frequency of 15 Hz are insensitive to long-period waves and that the multiplicative effect of correlation between two 15 Hz sensors diminishes the amplitude response at these periods. The dominance of instrument noise at long periods of these sensors can also mask the true signals, producing a seemingly more diffuse ASF. This could also explain why correlations between the shallow borehole stations and the deep borehole stations at frequencies less than 0.5 Hz were not successful.

Retrieved Wavefield at Reservoir Depth

We cross-correlated the data between the two deep boreholes SDM and ZRP that were recorded during days 326–357 of the year 2013. Here, correlation functions were obtained following the scheme of Liu *et al.* (2016), in which earthquakes are removed as statistical outliers (see Appendix D). We present results for the vertical (ZZ) and the radial (RR) components in Figure 10. For the TT component, the signal is much weaker and is not as informative as for the ZZ or RR components, so we focus on these two.

On the vertical component, three wave packets with coherent phases on most of the correlations are observed. The reservoir has a lower velocity than the layers immediately above and below (Fig. 2), and because most of the deep borehole stations are within the reservoir (Fig. 1), these wave packets are likely related to nearly horizontally propagating, reservoir-trapped *SV* waves. This feature is well observed in Figure 10, in which station pairs inside the reservoir have higher amplitudes than the pairs at the edge of the reservoir. This is typical amplitude behavior of a trapped wave in a waveguide (reservoir or fault zone) and is analogous to guided waves observed traveling inside of a low-velocity fault zone bounded by higher-velocity rocks (e.g., Ben-Zion *et al.*, 2003; Hillers *et al.*, 2014). To our knowledge, this observation is the first of its kind in a gas reservoir using ASF. We do not invert for the physical parameters of the reservoir here, because it requires rigorous modeling of the trapped wave that is beyond the scope of this study. For the radial component, the strongest arrivals peak clearly around −1 s; however, the phase arrivals are not as well aligned as for the ZZ component (Fig. 10c,f and Ⓔ Fig. S1, available in the electronic supplement to this article). This suggests that some of these phases may be refracted waves traveling in the fast layers immediately above or below the reservoir. Based on the peak envelope of these arrivals, the velocities of such waves range between 3.34 and 2.41 km/s (Ⓔ Fig. S1). It likely corresponds to the upper and lower bounding layers of the reservoir. According to the velocity model in Figure 2, the layer depth and thickness varies with location. Therefore, the ray paths between the fast layer and the sensors are different and not horizontal, which could explain the perturbations in phase arrival times, as well as the fact that those phases appear stronger on the radial-component correlation functions.

Another interesting feature of the correlation functions is their lack of symmetry, especially for the RR component. Such asymmetry is most likely related to the ASF source azimuth distribution at the 0.5–5 Hz frequency range. Although the ASF source distribution at the reservoir depth is unknown, results shown in the Beamforming section suggest that the ASF sources in the northeast direction are stronger, producing stronger phases from ZRP to SDM than in the opposite direction.

In traditional ASF interferometry, the vertical-component cross correlation and radial-component cross correlation are generally similar because they both record the Rayleigh waves with high amplitude. The strong distinction in waveforms between the vertical and radial components observed here adds

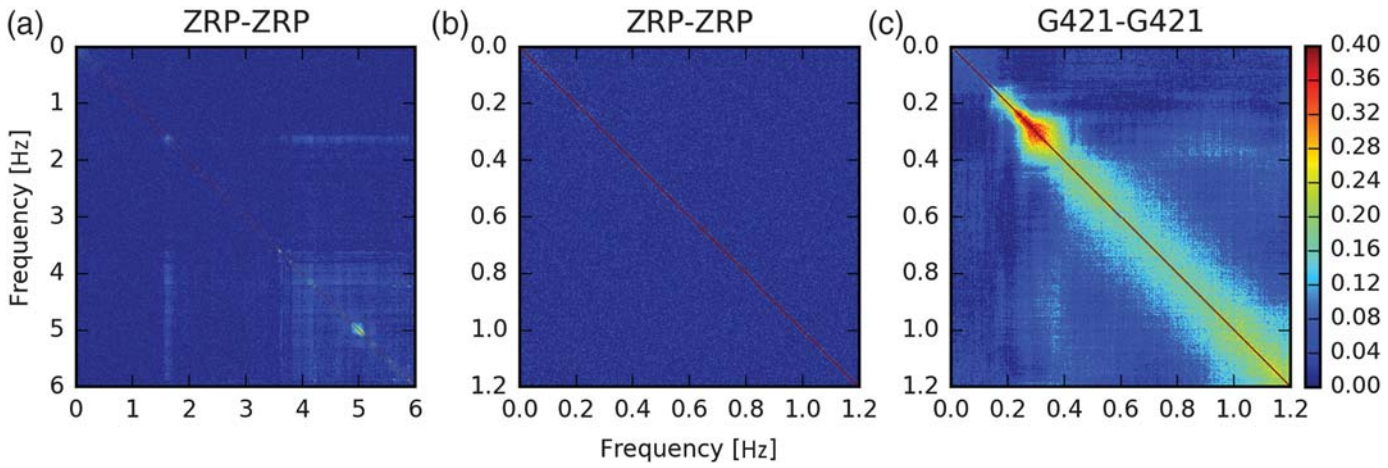

▲ **Figure 9.** (a) Correlation matrix of power spectral values at neighboring frequencies between 0 and 6 Hz for station ZRP–01 at 2.8 km depth. (b) Zoom of (a) in the spectral values between 0 and 1.2 Hz (ZZ). (c) Correlation matrix of power spectral values between 0 and 1.2Hz for station G421 at 50 m depth.

weight to our interpretation that they are dominated by different wave types following different ray paths: the reservoir-guided *SV* wave for the vertical component and the refracted shear wave in the fast layer for the radial component.

All these observations reinforce the idea that high-frequency ASF is present at reservoir depth but that its characteristics differ strongly from ASF at the surface.

DISCUSSION AND CONCLUSION

By means of beamforming, analysis of retrieved Green's functions from cross correlation, surface-wave eigenfunction analysis, and neighboring frequency correlations, we were able to determine the main characteristics of the ASF, including the predominant propagation modes and phases, measured over the Groningen area.

In the near surface and at long period, the ASF appears directional and not fully diffuse. Previous results suggest that the predominant sources of ASF come from the North Sea and the British coast; however, further analysis should be performed to confirm this conjecture. At higher frequencies, ASF sources appear more heterogeneous, likely having an anthropogenic origin.

Using different arrays located at the surface or using the shallow borehole array, we were able to retrieve clear Rayleigh, Love, and *P* waves from cross correlations of the ASF (Table 1). Using short offset arrays, we were able to retrieve up to the second-higher mode and third-higher mode for Rayleigh and Love waves, respectively. In agreement with the eigenfunction analysis, correlation functions show that the surface waves have higher energy in the near-surface layers. This energy quickly decreases with depth, as expected, which helps us observe *P* waves at the 200 m borehole level.

At reservoir depth, the surface-wave eigenfunction behavior also explains why

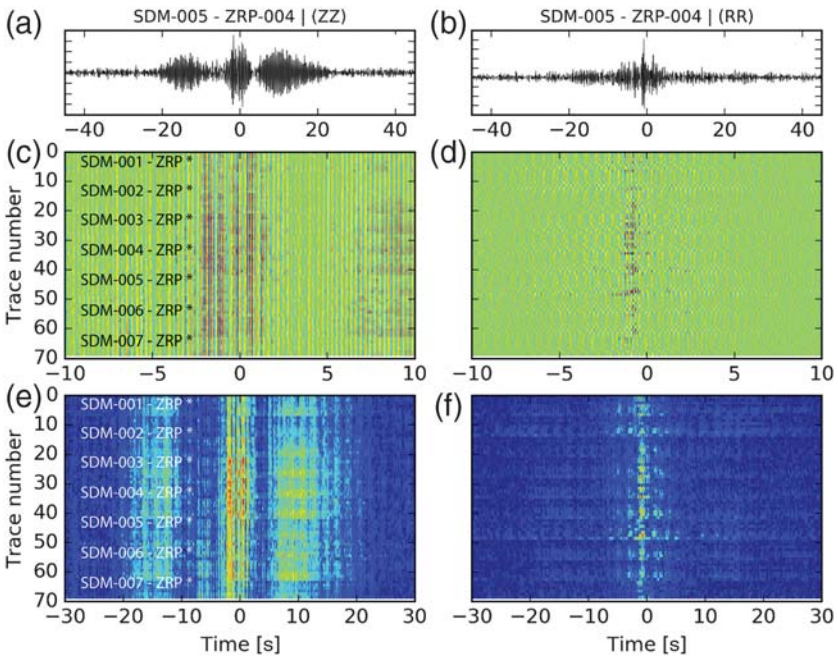

▲ **Figure 10.** Cross-correlation functions between the two deep borehole arrays (SDM and ZRP), band-pass filtered between 0.5 and 5 Hz. Amplitude balance is preserved for all correlation pairs. The left column shows the vertical-component (ZZ) correlations, and the right column shows the radial (RR) correlations. (a,b) example of one single correlation function (SDM–010 vs. ZRP-004). (c,d) All the correlation functions between SDM and each station in ZRP. Traces 1–10 are cross correlations between SDM array and ZRP-001; 11–20 are between SDM and ZRP-002; etc. (e) Cross-correlation envelope functions of all the correlation functions shown in (c,d).

high-frequency (> 0.5 Hz) correlations between the reservoir and the shallow surface were unsuccessful. On the other hand, although diving *P* waves are well observed in shallow boreholes, no such phases are observed at reservoir depth or between the surface and the reservoir. This is surprising because receivers at depth are potentially better suited to retrieve body waves because of the strong attenuation of the surface wave.

Zhou and Paulssen (2017) showed that high-frequency ASF is present at reservoir depth and that it originates mainly from the surface. By applying borehole interferometry using the SDM array, they were able to retrieve both *P*- and *S*- wave arrivals above 3 Hz. Even if high-frequency ASF at reservoir depth is likely originating from anthropogenic sources at the surface and borehole (as suggested by Zhou and Paulssen, 2017), our results suggest that the ASF content between the shallow surface and the reservoir is strongly different, which would render the monitoring of the reservoir using borehole-surface interferometry problematic.

Analysis of neighborhood frequencies at reservoir depth along with the correlation functions obtained between the two deep borehole arrays suggest that heterogeneous velocity structure strongly influences the ASF inside the reservoir. Within the reservoir, the high-frequency ASF appears trapped and refracted at depth across geological boundaries such as the basal anhydrite layer. The observation of reservoir-guided and refracted waves through seismic interferometry are the first of their kind in an active-production reservoir environment. Although they are promising for structural characterization of the reservoir (e.g., Hillers *et al.*, 2014), they also highlight the difficulties and challenges of monitoring the reservoir *in situ* using ASF observations.

Finally, by offering an overall view of the different possibilities that offer ASF correlations with several arrays, we hope this research will help guide future efforts to recover structural information at Groningen.

DATA AND RESOURCES

The data used in this study were acquired by Royal Netherlands Meteorological Institute (KNMI), Nederlandse Aardolie Maatschappij (NAM), and Shell Global Solutions International B.V. The G-array data and metadata are available without restrictions from the KNMI website (http://rdsa.knmi.nl/dataportal/, last accessed May 2018). Most of the figures have been plotted with Matplotlib (Hunter, 2007), and some of the data processing steps have been performed using ObsPy (Beyreuther *et al.*, 2010) and pyrocko (http://pyrocko.org/, last accessed May 2018). The other information is from the Dinoloket website available at https://www.dinoloket.nl/en/ (last accessed May 2018).

ACKNOWLEDGMENTS

The authors thank the staff of Nederlandse Aardolie Maatschappij (NAM), Royal Netherlands Meteorological Institute (KNMI) and Shell Global Solutions International B.V. for data acquisition, management, and distribution. The authors thank Indrajit Das who provided us the data of the temporary arrays. This research was funded by Shell Global Solutions International B.V. The authors are grateful for thorough reviews of Elmer Ruigrok, two anonymous referees and for the editorial work of Zhigang Peng and Brandon Schmandt.

REFERENCES

Aki, K., and P. Richards (2002). *Quantitative Seismology*, University Science Book, California.

Behm, M. (2017). Feasibility of borehole ambient noise interferometry for permanent reservoir monitoring, *Geophys. Prospect.* **65,** no. 2, 563–580.

Ben-Zion, Y., Z. Peng, D. Okaya, L. Seeber, J. G. Armbruster, N. Ozer, A. J. Michael, S. Baris, and M. Aktar (2003). A shallow fault-zone structure illuminated by trapped waves in the Karadere–Duzce branch of the north Anatolian fault, western Turkey, *Geophys. J. Int.* **152,** no. 3, 699–717.

Bensen, G. D., M. H. Ritzwoller, and N. M. Shapiro (2008). Broadband ambient noise surface wave tomography across the United States, *J. Geophys. Res.* **113,** no. B5, doi: 10.1029/2007JB005248.

Beyreuther, M., R. Barsch, L. Krischer, T. Megies, Y. Behr, and J. Wassermann (2010). ObsPy: A Python toolbox for seismology, *Seismol. Res. Lett.* **81,** no. 3, 530–533, doi: 10.1785/gssrl.81.3.530.

Bommer, J. J., P. J. Stafford, B. Edwards, B. Dost, E. van Dedem, A. Rodriguez-Marek, P. Kruiver, J. van Elk, D. Doornhof, and M. Ntinalexis (2017). Framework for a ground-motion model for induced seismic hazard and risk analysis in the Groningen gas field, the Netherlands, *Earthq. Spectra* **33,** no. 2, doi: 10.1193/082916EQS138M.

Bonnefoy-Claudet, S., F. Cotton, and P.-Y. Bard (2006). The nature of noise wavefield and its applications for site effects studies: A literature review, *Earth Sci. Rev.* **79,** nos. 3/4, 205–227, doi: 10.1016/j.earscirev.2006.07.004.

Claerbout, J. (2014). *Geophysical Image Estimation by Example*, Lulu.com, 251 pp.

De Mulder, E. F., M. C. Geluk, I. Ritsema, W. E. Westerhoff, and T. E. Wong (2003). *De ondergrond van Nederland*, Wolters-Noordhoff, Groningen/Houten, The Netherlands, 379 pp. (in Dutch).

Denolle, M. A., E. M. Dunham, and G. C. Beroza (2012). Solving the surface-wave eigenproblem with Chebyshev spectral collocation, *Bull. Seismol. Soc. Am.* **102,** no. 3, 1214–1223.

Douze, E. (1967). Short-period seismic noise, *Bull. Seismol. Soc. Am.* **57,** no. 1, 55–81.

Gupta, I. N. (1965). Standing-wave phenomena in short-period seismic noise, *Geophysics* **30,** no. 6, 1179–1186.

Hillers, G., and M. Campillo (2016). Fault zone reverberations from cross-correlations of earthquake waveforms and seismic noise, *Geophys. J. Int.* **204,** no. 3, 1503–1517.

Hillers, G., M. Campillo, Y. Ben-Zion, and P. Roux (2014). Seismic fault zone trapped noise, *J. Geophys. Res.* **119,** no. 7, 5786–5799.

Hillers, G., S. Husen, A. Obermann, T. Planès, E. Larose, and M. Campillo (2015). Noise-based monitoring and imaging of aseismic transient deformation induced by the 2006 Basel reservoir stimulation, *Geophysics* **80,** no. 4, KS51–KS68.

Hofman, L., E. Ruigrok, B. Dost, and H. Paulssen (2017). A shallow seismic velocity model for the Groningen area in the Netherlands, *J. Geophys. Res.* **122,** no. 10, 8035–8050, doi: 10.1002/2017JB014419.

Hunter, J. D. (2007). Matplotlib: A 2D graphics environment, *Comput. Sci. Eng.* **9,** no. 3, 90–95, doi: 10.1109/MCSE.2007.55.

Kay, S. M. (1988). *Modern Spectral Estimation*, Pearson Education India.

Kimman, W., X. Campman, and J. Trampert (2012). Characteristics of seismic noise: Fundamental and higher mode energy observed in the northeast of the Netherlands, *Bull. Seismol. Soc. Am.* **102,** no. 4, 1388–1399.

Kruiver, P. P., E. van Dedem, R. Romijn, G. de Lange, M. Korff, J. Stafleu, J. L. Gunnink, A. Rodriguez-Marek, J. J. Bommer, J. van Elk, *et al.* (2017). An integrated shear-wave velocity model for the Groningen gas field, the Netherlands, *Bull. Earthq. Eng.* **15,** no. 9, 3555–3580.
Lacoss, R., E. Kelly, and M. Toksöz (1969). Estimation of seismic noise structure using arrays, *Geophysics* **34,** no. 1, 21–38, doi: 10.1190/1.1439995.
Liu, X., and Y. Ben-Zion (2016). Estimating correlations of neighbouring frequencies in ambient seismic noise, *Geophys. J. Int.* **206,** no. 2, 1065–1075.
Liu, X., Y. Ben-Zion, and D. Zigone (2016). Frequency domain analysis of errors in cross-correlations of ambient seismic noise, *Geophys. Suppl. Month. Notices Roy. Astron. Soc.* **207,** no. 3, 1630–1652.
Miyazawa, M., R. Snieder, and A. Venkataraman (2008). Application of seismic interferometry to extract *P*- and *S*-wave propagation and observation of shear-wave splitting from noise data at Cold Lake, Alberta, Canada, *Geophysics* **73,** no. 4, D35–D40.
Nakata, N., J. P. Chang, J. F. Lawrence, and P. Boué (2015). Body wave extraction and tomography at Long Beach, California, with ambient-noise interferometry, *J. Geophys. Res.* **120,** no. 2, 1159–1173, doi: 10.1002/2015JB011870.
Nakata, N., R. Snieder, S. Kuroda, S. Ito, T. Aizawa, and T. Kunimi (2013). Monitoring a building using deconvolution interferometry. I: Earthquake-data analysis, *Bull. Seismol. Soc. Am.* **103,** no. 3, 1662–1678.
Nishida, K., J.-P. Montagner, and H. Kawakatsu (2009). Global surface wave tomography using seismic hum, *Science* **326,** no. 5949, 112, doi: 10.1126/science.1176389.
Noorlandt, R., P. P. Kruiver, M. P. de Kleine, M. Karaoulis, G. de Lange, A. Di Matteo, J. von Ketelhodt, E. Ruigrok, B. Edwards, A. Rodriguez-Marek, *et al.* (2018). Characterisation of ground motion recording stations in the Groningen gas field, *J. Seismol.* 1–19, doi: 10.1007/s10950-017-9725-6.
Peterson, J. (1993). Observations and modeling of seismic background noise, *U.S. Geol. Surv. Open-File Rept. 95-322*.
Poli, P., M. Campillo, H. Pedersen, and LAPNET Working Group (2012). Body-wave imaging of Earth's mantle discontinuities from ambient seismic noise, *Science* **338,** no. 6110, 1063–1065.
Roux, P., K. G. Sabra, P. Gerstoft, W. A. Kuperman, and M. C. Fehler (2005). *P*-waves from cross-correlation of seismic noise, *Geophys. Res. Lett.* **32,** L19303, doi: 10.1029/2005GL023803.
Royal Netherlands Meteorological Institute (KNMI) (1993). *Netherlands Seismic and Acoustic Network*, Royal Netherlands Meteorological Institute (KNMI), Other/Seismic Network, doi: 10.21944/e970fd34-23b9-3411-b366-e4f72877d2c5.
Ruigrok, E., X. Campman, and K. Wapenaar (2011). Extraction of P-wave reflections from microseisms, *Compt. Rendus Geosci.* **343,** nos. 8/9, 512–525, doi: 10.1016/j.crte.2011.02.006.
Ruigrok, E., J. Paulssen, and J. Trampert (2015). *Tremor Mapping at the Groningen Field*, available at http://www.seismo.ethz.ch/en/static/schatzalp/2015/S6P13_Ruigrok.pdf (last accessed May 2018).
Sánchez-Sesma, F. J., and M. Campillo (2006). Retrieval of the Green's function from cross correlation: The canonical elastic problem, *Bull. Seismol. Soc. Am.* **96,** no. 3, 1182–1191, doi: 10.1785/0120050181.
Shapiro, N. M., and M. Campillo (2004). Emergence of broadband Rayleigh waves from correlations of the ambient seismic noise, *Geophys. Res. Lett.* **31,** no. 7, doi: 10.1029/2004GL019491.
Shapiro, N. M., M. Campillo, L. Stehly, and M. H. Ritzwoller (2005). High-resolution surface-wave tomography from ambient seismic noise, *Science* **307,** no. 5715, 1615–1618, doi: 10.1126/science.1108339.
Spica, Z., M. Perton, and G. C. Beroza (2017). Lateral heterogeneity imaged by small-aperture ScS retrieval from the ambient seismic field, *Geophys. Res. Lett.* **44,** no. 16, 8276–8284, doi: 10.1002/2017GL073230.
Spica, Z., M. Perton, and D. Legrand (2017). Anatomy of the Colima volcano magmatic system, Mexico, *Earth Planet. Sci. Lett.* **459,** 1–13, doi: 10.1016/j.epsl.2016.11.010.
Spica, Z. J., M. Perton, N. Nakata, X. Liu, and G. C. Beroza (2017). Site characterization at Groningen gas field area through joint surface-borehole H/V analysis, *Geophys. J. Int.* **212,** no. 1, 412–421, doi: 10.1093/gji/ggx426.
Spica, Z. J., M. Perton, N. Nakata, X. Liu, and G. C. Beroza (2018). Shallow V_S imaging of the Groningen area from joint inversion of multimode surface waves and H/V spectral ratios, *Seismol. Res. Lett.* doi: 10.1785/0220180060 (in press).
Stehly, L., M. Campillo, and N. M. Shapiro (2006). A study of the seismic noise from its long-range correlation properties, *J. Geophys. Res.* **111,** no. B10, doi: 10.1029/2005JB004237.
van Elk, J., D. Doornhof, J. J. Bommer, S. J. Bourne, S. J. Oates, R. Pinho, and H. Crowley (2017). Hazard and risk assessments for induced seismicity in Groningen, *Neth. J. Geosci.* **96,** no. 5, s259–s269.
van Thienen-Visser, K., and J. Breunese (2015). Induced seismicity of the Groningen gas field: History and recent developments, *The Leading Edge* **34,** no. 6, 664–671.
Vos, P. C. (2015). Origin of the Dutch coastal landscape, in *Long-Term Landscape Evolution of the Netherlands during the Holocene, Described and Visualized in National, Regional and Local Palaeogeographical Map Series*, Barkhuis Publishing, Eelde, The Netherlands.
Wapenaar, K., and J. Fokkema (2006). Green's function representations for seismic interferometry, *Geophysics* **71,** no. 4, SI33–SI46.
Zhou, W., and H. Paulssen (2017). *P* and *S* velocity structure in the Groningen gas reservoir from noise interferometry, *Geophys. Res. Lett.* **44,** no. 23, 11,785–11,791, doi: 10.1002/2017GL075592.
Zöller, G., and M. Holschneider (2016). The maximum possible and the maximum expected earthquake magnitude for production-induced earthquakes at the gas field in Groningen, the Netherlands, *Bull. Seismol. Soc. Am.* **106,** no. 6, 2917–2921.

APPENDIX A

POWER SPECTRAL DENSITIES

Because of the vicinity to the coast, the power spectral density (PSD) of ground motion at the microseismic peak is generally high (Fig. A1). This characteristic is clear for sensors at the surface, such as the Wittewierum and the Loppersum arrays. Because the Wittewierum and Loppersum arrays were installed during the winter, the strong energy from storms might cause the observations to exceed the high-noise model of Peterson (1993). The accelerometers appear to have relatively high intrinsic noise levels compared to the geophones. This may be due to the fact that they are mainly used as strong-motion sensors and therefore have low gain to remain on scale during strong shaking. Sensors at shallow depth from the G-array show slightly lower noise level. The deep borehole SDM is extremely stable in time but shows poor sensitivity to ground movements under 10 Hz, whereas other stations appear to successfully record ground movements down to at least 0.1 Hz.

APPENDIX B

ARRAY RESPONSE

We compute the frequency–slowness response of the arrays to assess the resolution and then the accuracy of the beamforming results shown in Figure 3. Figure B1 shows the responses for the different arrays and frequencies in a similar representation as in Figure 3. We use a monochromatic plane wave arriving

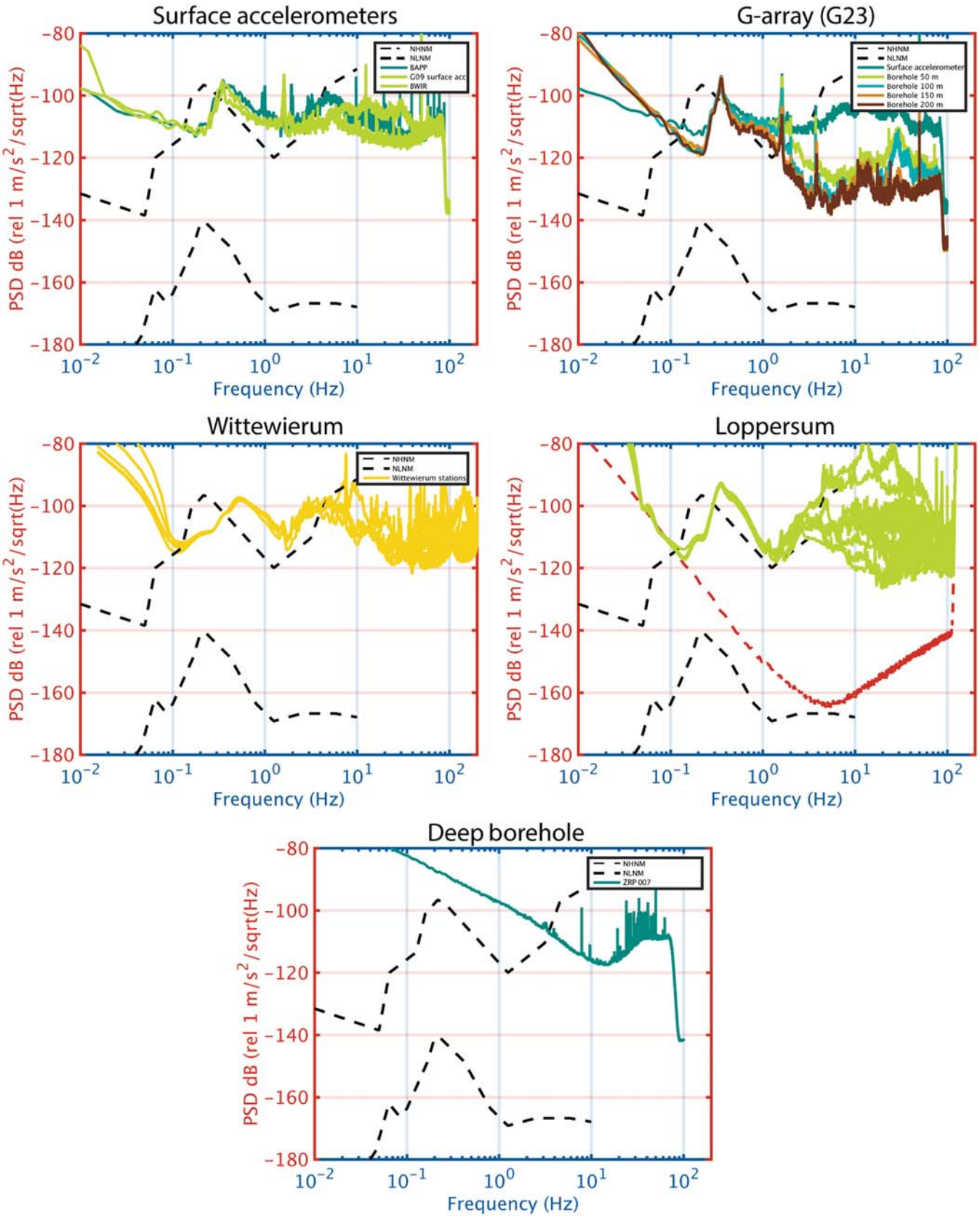

▲ **Figure A1.** Power spectral density (PSD) function analysis for different stations of arrays at Groningen. Black lines are the high-noise and low-noise model of Peterson (1993). The red curve in the Loppersum array plot is the PSD of instrument noise. The crossover point between electronic and ambient seismic noise lies at about 8 s.

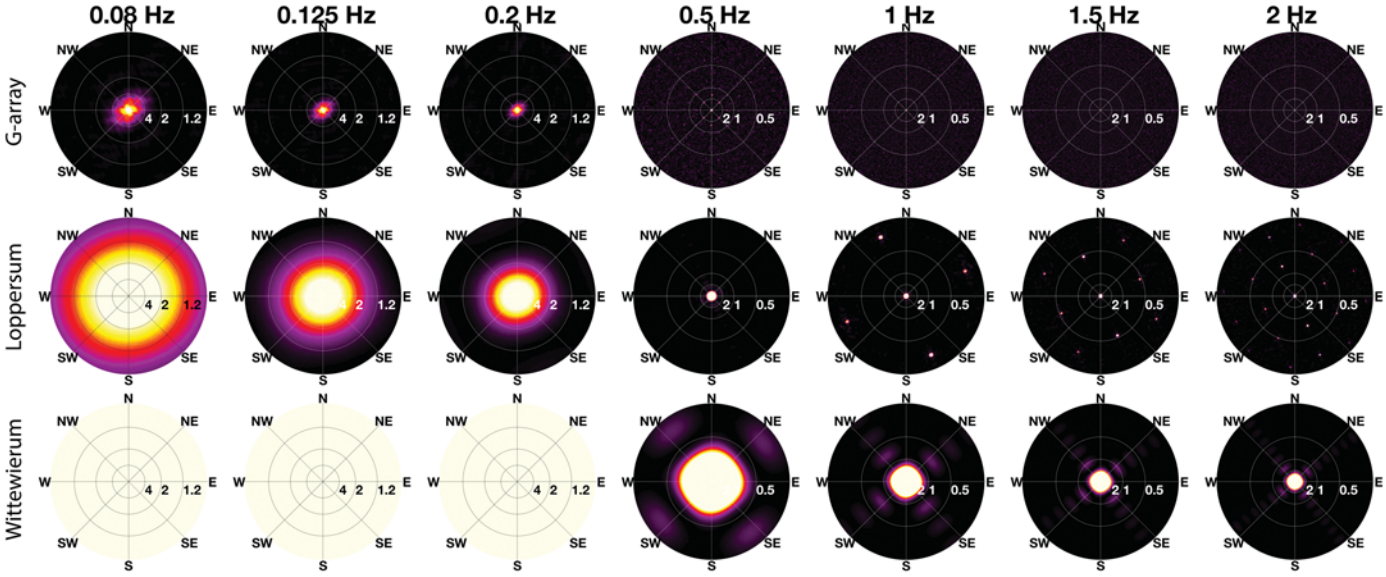

▲ **Figure B1.** Frequency–slowness responses of the three different arrays as for Figure 3. The amplitudes of these spectra are preserved (not normalized at each panel). For the Wittewierum array, the wavelength is too long to have any resolution for low-frequency ranges.

with infinite velocity (i.e., a vertical incident synthetic sine wave). The real signal is located at the center of this slowness diagram, and the size and location of bright spots show the response of the array at each frequency. These tests demonstrated that lower frequencies (0.08–0.2 Hz) are better sampled by the G-array. Intermediate frequencies (0.5 and 1.0 Hz) are better sampled by the Loppersum array, whereas the G-array has strong aliasing effects, and the Wittewierum array does not have enough resolution. Note that the Loppersum array shows aliasing at 1 Hz, but the real and pseudosignals are still clearly separated, and we can easily distinguish them, as shown in Figure 3. Higher frequencies (1.5 and 2.0 Hz) are better sampled with the Wittewierum array. The Loppersum array is probably still useful, but we need to be careful not to interpret aliased signals as secondary sources.

APPENDIX C

SURFACE-WAVE EIGENPROBLEM

Following Denolle *et al.* (2012), the surface-wave eigenproblem can be treated using the system of equations of surface-wave components in a 1D elastic medium:

$$\mathbf{L}\mathbf{v} = k\mathbf{v}, \tag{C1}$$

in which the linear differential operator $\mathbf{L}$ contains the depth derivative d/dz and frequency ω, the eigenvector $\mathbf{v}$ contains displacement field u and certain stress components and is a function of depth, and the eigenvalue k is the horizontal wavenumber.

We are interested in the displacement field in the eigenvector solution. In a cylindrical coordinate system, the displacement field has the specific form of

$$u = [r_1(k,z,\omega)\mathbf{S}_k^m(r,\phi) + l_1(k,z,\omega)\mathbf{T}_k^m(r,\phi) + ir_2(k,z,\omega)(R)_k^m(r,\phi)]e^{i\omega t} \tag{C2}$$

(Aki and Richards, 2002), in which the scalar displacement eigenfunctions $r_1(k,z,\omega)$ and $r_2(k,z,\omega)$ are for Rayleigh waves, and $l_1(k,z,\omega)$ are for Love waves. The three orthogonal basis vectors $\mathbf{S}_k^m(r,\phi)$, $\mathbf{T}_k^m(r,\phi)$, and $\mathbf{R}_k^m(r,\phi)$ are related to cylindrical harmonics of order m and wavenumber k. More details can be found in Denolle *et al.* (2012). For Rayleigh waves, equation (C2) indicates that there is $\pi/2$ phase shift between the horizontal component r_1 and vertical component r_2.

APPENDIX D

CORRELATION OF NEIGHBORHOOD FREQUENCIES ANALYSIS

Here, we briefly describe the data processing steps for computing the correlation of neighboring frequencies. Commonly used preprocessing methods, such as 1-bit normalization and spectral whitening, modify the statistics of noise recording nonlinearly and can produce spurious results in the correlation matrix. Therefore, we cannot apply those preprocessing steps in our analysis.

We follow Liu *et al.* (2016), in which earthquakes are removed as statistical outliers. We first divide the time series into evenly spaced 200 s windows. Then, we compute the power spectra for each time window and remove outliers based on four times the median absolute deviation of the distribution of spectrum values at each frequency. An abnormal window (e.g., one containing an earthquake) contains more than 8% outliers among all frequencies. After removing abnormal windows, we compute correlation coefficients of neighboring

power spectral values based on the selected windows as in Liu and Ben-Zion (2016)

$$\mathrm{Corr}[|\psi(\mathbf{r},f_p)|^2,|\psi(\mathbf{r},f_q)|^2]=\frac{\mathrm{Cov}[|\psi(\mathbf{r},f_p)|^2,|\psi(\mathbf{r},f_q)|^2]}{\sqrt{\mathrm{Var}[|\psi(\mathbf{r},f_p)|^2]\mathrm{Var}[|\psi(\mathbf{r},f_q)|^2]}}, \quad \text{(D1)}$$

in which $|\psi(\mathbf{r},f_p)|^2$ is the power spectrum at frequency f_p. Here, Cov and Var represent covariance and variance, respectively.

Zack J. Spica
Xin Liu
Gregory C. Beroza
Department of Geophysics
397 Panama Mall
Stanford University
Stanford, California 94305-2215 U.S.A.
zspica@stanford.edu

Nori Nakata
ConocoPhillips School of Geology and Geophysics
University of Oklahoma
Norman, Oklahoma U.S.A.

Xander Campman
Zijian Tang
Shell Global Solutions International B.V.
Amsterdam, The Netherlands

Published Online 30 May 2018